Supporting Information

Porous $Ni_{1-x}Cu_xO$ Nanowire Arrays as Noble-Metal-Free High-Performance Catalysts for Ammonia-Borane Electrooxidation

Chengqi Wu, Jie Zhu, Hu Wang, Guojing Wang, Tao Chen, and Yiwei Tan*

State Key Laboratory of Materials-Oriented Chemical Engineering, School of Chemistry and Chemical Engineering, Nanjing Tech University, Nanjing 211816, China, Email: ytan@njtech.edu.cn

Experimental Section

Synthesis

Materials. Nickel(II) chloride hexahydrate ($NiCl_2·6H_2O$, 99%), copper(II) chloride dihydrate ($CuCl_2·2H_2O$, 99%), urea (NH_2CONH_2, 99%), ammonia-borane (NH_3BH_3, 97%), nitric acid (HNO_3, 68–70%), cupric oxide (CuO, 99%), and potassium hydroxide (KOH, 99.9%) were commercially available from Sinopharm Chemical Reagent Co., Ltd.. Carbon fiber paper (CFP, ~180 μm in thickness) and carbon supported platinum catalyst (Pt/C, 60 wt% of Pt nanoparticles with size smaller than 7 nm) were purchased from Wuhan Cetech Co., Ltd.. and Shanghai Hesen Electric Co., Ltd, respectively. All reagents were used without any further purification. Ultrapure water (18.2 MΩ) produced with a Milli-Q purification system was used in the synthesis and all the electrochemical measurements. CFP was thoroughly washed by sonication in isopropanol and then in water alternatively for three times, and then pretreated with concentrated nitric acid (68–70%) at the 75 °C for 90 min to achieve the surface hydroxylation of CFP. After being washed with water, the pretreated CFP was used as the support for synthesizing the integrated p-$Ni_{1-x}Cu_xO$/CFP catalysts.

Characterization of Materials

Scanning electron microscopy (SEM) images and near-surface elemental mapping data were acquired using a Hitachi S-4800 field-emission scanning electron microscope equipped with an energy-dispersive X-ray (EDX) spectroscopy detector (Oxford) and operated at an accelerating voltage of 5 and 20 kV to probe the morphology and near-surface chemical composition of the catalysts, respectively. Transmission electron microscopy (TEM) micrographs were obtained using an FEI Tecnai G2 Spirit Bio TWIN transmission electron microscope operated at an accelerating voltage of 100 kV. High-resolution TEM (HRTEM) and scanning TEM (STEM) micrographs, and high-angle annular dark field (HAADF)-STEM elemental maps were acquired using an FEI ETEM Titan G2 60-300 Cs-corrected scanning transmission electron microscope equipped with a spherical aberration corrector for the electron beam, a HAADF detector for STEM imaging, and an Oxford INCA EDS detector and operated at 300 kV to analyze the crystallographic structure and composition of samples. STEM micrographs and elemental maps were obtained in HAADF mode to provide the bulk chemical composition of samples. The specimens for TEM observations and HRTEM analyses were carefully scratched from the CFP support and sonicated before dropping them onto 300 mesh carbon-coated molybdenum grids. The metallic composition of the catalyst was also determined by inductively coupled plasma-optical emission spectrometry (ICP-OES, Prodigy, Leeman Labs Inc., λ = 165–800 nm, As = 200 nm) measurements after dissolving the sample in aqua regia. To obtain the phase and structure of samples, the X-ray diffraction (XRD) patterns were collected using a Rigaku SmartLab diffractometer with a Cu Kα X-ray source (λ = 1.54056 Å, generated at 40 kV and 100 mA) and recorded in a collection mode of 12 s per step and a step size of 0.02° in the 2θ range from 10° to 110° in the Rietveld routine. Rietveld refinement was performed using the FULLPROF program to refine the scale factor, zero shifting, unit cell parameter, peak asymmetry, background, and profile parameters. The CFP coated with an active material was directly used as the specimen for XRD characterization after cleaning treatment. To evaluate the surface composition and elemental oxidation states of samples, X-ray photoelectron spectroscopy (XPS) measurements were

carried out using a PHI5000 VersaProbe (ULVAC-PHI) spectrometer with a hemispherical energy analyzer and a monochromatized microfocused Al-Kα (hv = 1486.58 eV) X-ray source. Samples for XPS measurements were carefully scratched from the CFP support and then sputtered by repeated cycles of Ar^+ ions to obtain clean sample surfaces. The binding energies (BEs) of the core levels were calibrated by setting the adventitious C 1s peak at 284.8 eV. Survey spectra of the samples in the BE range of 0–1000 eV and the core level spectra of the elemental signals were collected with a step size of 1 and 0.125 eV, respectively. Nitrogen adsorption–desorption isotherms were measured by nitrogen physisorption at 77 K using a BELSORP mini II apparatus (Bel Inc.). To determine the specific surface areas (S_{BET}) and pore size distributions of the samples, the Brunauer–Emmett–Teller (BET) method based on the adsorption data of the corresponding N_2 isotherm in the relative pressure (P/P_0) range from 0.04 to 0.20 and the Barrett-Joyner-Halenda (BJH) method by using nitrogen adsorption data, respectively. The samples were degassed under high vacuum (< 0.01 mbar) at 150 °C for at least 6 h prior to the measurements.

Additional Discussion

EIS Measurements. The EIS measurements were carried out by sampling 100 points in the frequency range from 100 kHz to 0.1 Hz with an AC perturbation of 5 mV at room temperature. The complex nonlinear least square fitting (CNLS) of all the EIS spectra is conducted with the Zview 3.1 software package. The fitted electric equivalent circuit (EEC) is the two-time constant serial model (2TS) including a solution resistance (R_s), a resistance of the solution filling pores (R_1), one constant phase element (CPE_1) replacing the pore capacitance C_p, a charge transfer resistance (R_{ct}), the other CPE_2 replacing the interface capacitance C_{int} (i.e., R_s, R_{por}||CPE_1 and R_{ct}||CPE_2, the left inset in Figure 2d).[1–3] Figure 2d shows the Nyquist plots (symbols) of EIS centered at −0.10 V_{RHE} according to modeling with the corresponding EEC, revealing the presence of two overlapped semicircles at high frequencies (HF) and low frequencies (LF). Concomitantly, there is an excellent agreement between the experimental data (symbols) and CNLS approximations (solid lines) when the 2TS model is applied (Figure 2d).

The Calculation of TOF. The electrochemical accessible surface area (A_{ECSA}) was calculated based on the scan rate dependence of the charging current density (Figure S9). The current value Δj in Figure S9b was obtained by adding the absolute values of the anodic and cathodic currents from the CV curves in Figure S9a at the corresponding intermediate applied potential. The slope of the Δj *vs*. scan rate plot is twice C_{dl} (*i.e.*, $C_{dl} = \Delta j/(2v) = 19.02$ mF cm^{-2}). This C_{dl} value is significantly larger than those of many previous porous catalysts, *e.g.*, Ni/Mo_2C-PC (11.2 mF cm^{-2}) and (Ni,Co)Se_2-GA (16.0 mF cm^{-2}),[4,5] indicating that adequate active sites are available on the p-$Ni_{1-x}Cu_xO$ surface to ensure the improvement of catalytic activity, while A_{ECSA} is not the only descriptor for this. Thus, A_{ECSA} can be calculated based on Eq. S1 and the specific capacitances (C_s) in 1 M KOH ($C_s = 0.040$ mF cm^{-2}),[6] as shown in the following:

$$A_{\mathrm{ECSA}} = \frac{C_{\mathrm{dl}}}{C_{\mathrm{s}}} \quad \text{(S1)}$$

Thus, the obtained A_{ECSA} for the p-$Ni_{1-x}Cu_xO$/CFP electrode is 475.5 cm^2.

The TOF value was calculated according to the Eq. S2 shown below:

$$\mathrm{TOF} = \frac{JA\eta}{6FN_{\mathrm{ss}}} \quad \text{(S2)}$$

where J is the current density at 0.3 V_{RHE}, A is the geometrical area of the p-$Ni_{1-x}Cu_xO$/CFP electrode (1 cm^2), η is the FE of the ABOR derived from the preceding discussion (99%), the number 6 represents the 6-electron-involved reaction, F is the Faraday constant, and N_{ss} is the total molar number of active sites (Cu, Ni, and O) on the p-$Ni_{1-x}Cu_xO$/CFP surface. It is believed that no surface species are spectator during a catalytic reaction and they usually show synergistic effects on improving the electrocatalytic activity and therefore participate in the catalytic process together. Therefore, the number of active sites is the total number of surface Cu, Ni, and O ions.

The fcc $Ni_{1-x}Cu_xO$ contains 4 metallic ions and 4 oxygen ions in its unit cell and have a unit cell volume of 73.88 Å^3 on the basis of $a = 4.196$ Å. As a result, the total molar number of the surface sites on the real $Ni_{1-x}Cu_xO$ surface area is:

$$N_{\mathrm{SS}} = A_{\mathrm{ECSA}} \left(\frac{8 \text{ ions per unit cell}}{73.88 \text{ Å}^3 \text{per unit cell}} \right)^{\frac{2}{3}} \left(\frac{1}{N_{\mathrm{A}}} \right) \quad \text{(S3)}$$

where N_A is Avogadro's constant. Therefore, N_{ss} is calculated to be 1.794×10^{-6}. The obtained TOF values are listed in Table 1.

ABOR Mechanism. The ABOR mechanism involves the spontaneous generation of hydroxyborane anion (BH_3OH^-), B−H bond breaking steps (i.e., dehydrogenation) by the addition of OH^-, followed by the electrooxidation of the adsorbed hydrogen atoms in the presence of OH^-. The elementary steps are supposed to be via the five-coordinate intermediates and can be described by the following sequence (Eqs. S4−S14):

$$NH_3BH_3 * + OH^- = NH_3BH_3OH^- * \quad (S4)$$

$$NH_3BH_3OH^- * = NH_3 * + BH_3OH^- * \quad (S5)$$

$$BH_3OH^- * + OH^- = BH_3(OH)_2^{2-} * \quad (S6)$$

$$BH_3(OH)_2^{2-} * = BH_3(OH)_2^- * + e^- \quad (S7)$$

$$BH_3(OH)_2^- * = BH_2(OH)_2^- * + H * \quad (S8a)$$

$$H * + OH^- = H_2O + e^- \quad (S8b)$$

$$BH_2(OH)_2^- * + OH^- = BH_2(OH)_3^{2-} * \quad (S9)$$

$$BH_2(OH)_3^{2-} * = BH_2(OH)_3^- * + e^- \quad (S10)$$

$$BH_2(OH)_3^- * = BH(OH)_3^- * + H * \quad (S11a)$$

$$H * + OH^- = H_2O + e^- \quad (S11b)$$

$$BH(OH)_3^- * + OH^- = BH(OH)_4^{2-} * \quad (S12)$$

$$BH(OH)_4^{2-} * = BH(OH)_4^- * + e^- \quad (S13)$$

$$BH(OH)_4^- * = B(OH)_4^- * + H * \quad (S14a)$$

$$H * + OH^- = H_2O + e^- \quad (S14b)$$

where the * denotes the active sites on the surface of the p-$Ni_{1-x}Cu_xO$ NWs.

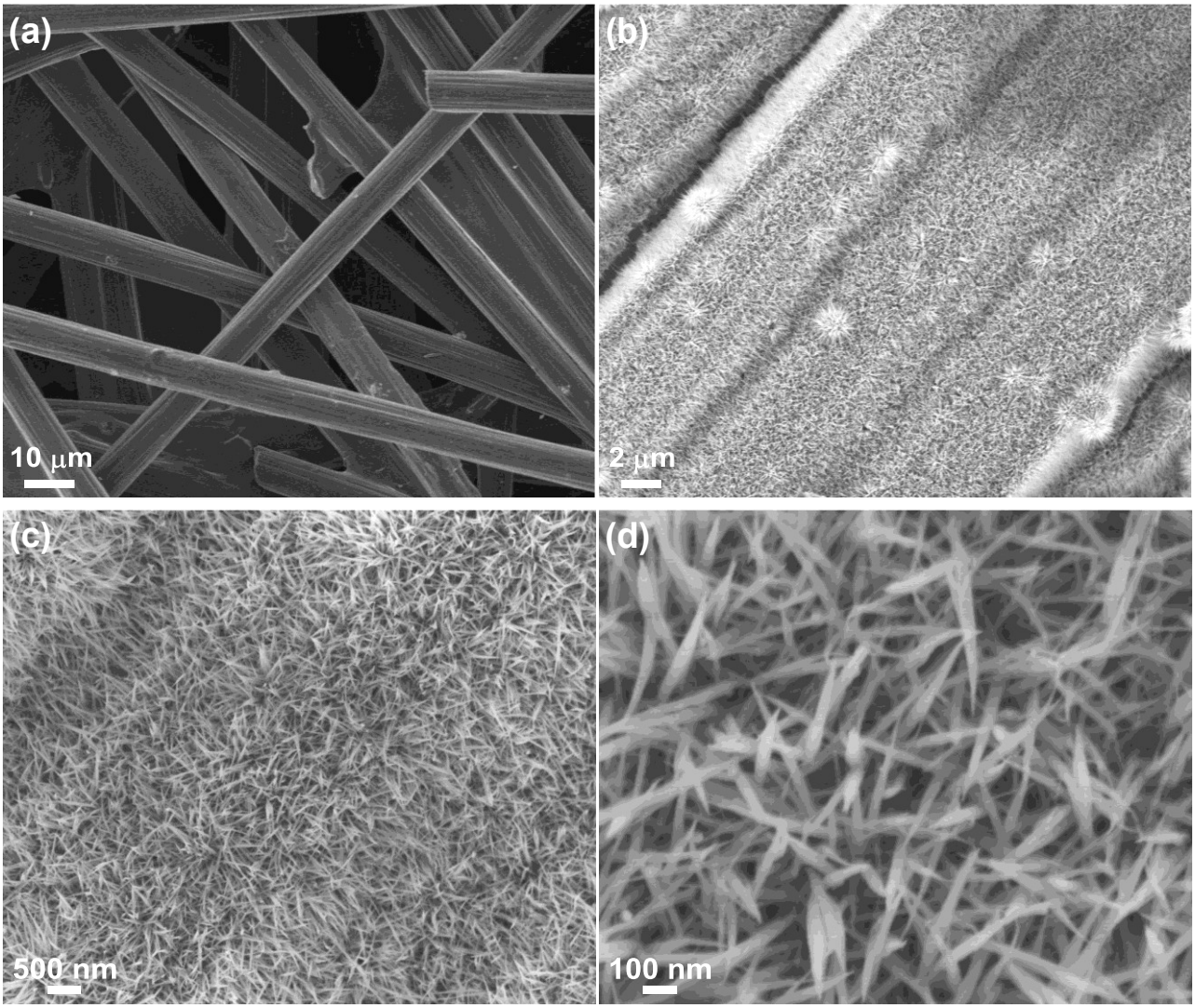

Figure S1. SEM micrographs of (a) the CFP substrate and (b−d) the Ni−Cu basic carbonate NWs/CFP precursor obtained at different magnifications.

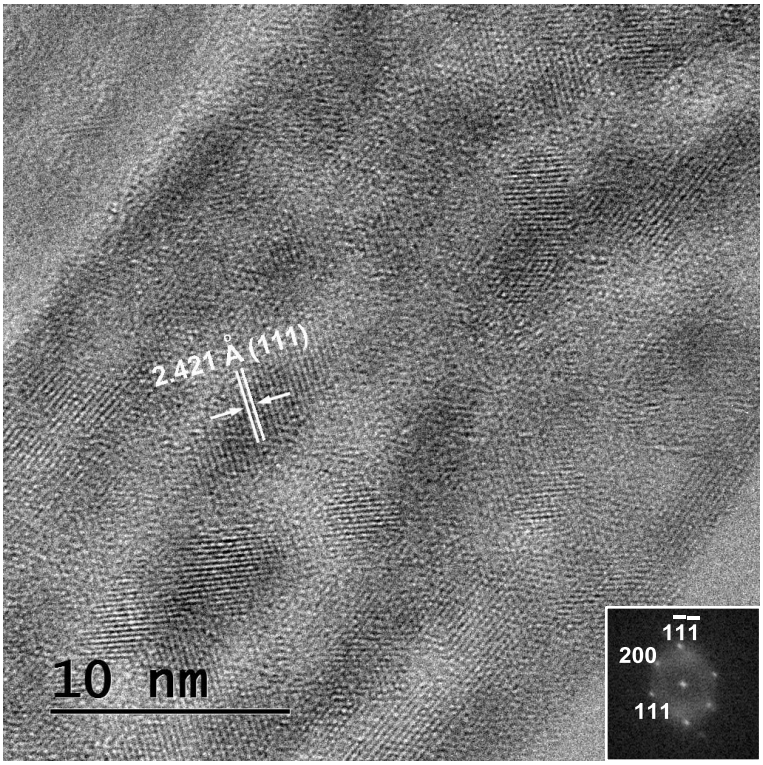

Figure S2. HRTEM micrograph of the p-$Ni_{1-x}Cu_xO$ NWs, showing the (111) planes of the cubic $Ni_{1-x}Cu_xO$ phase. The inset shows the corresponding fast Fourier transform (FFT) pattern.

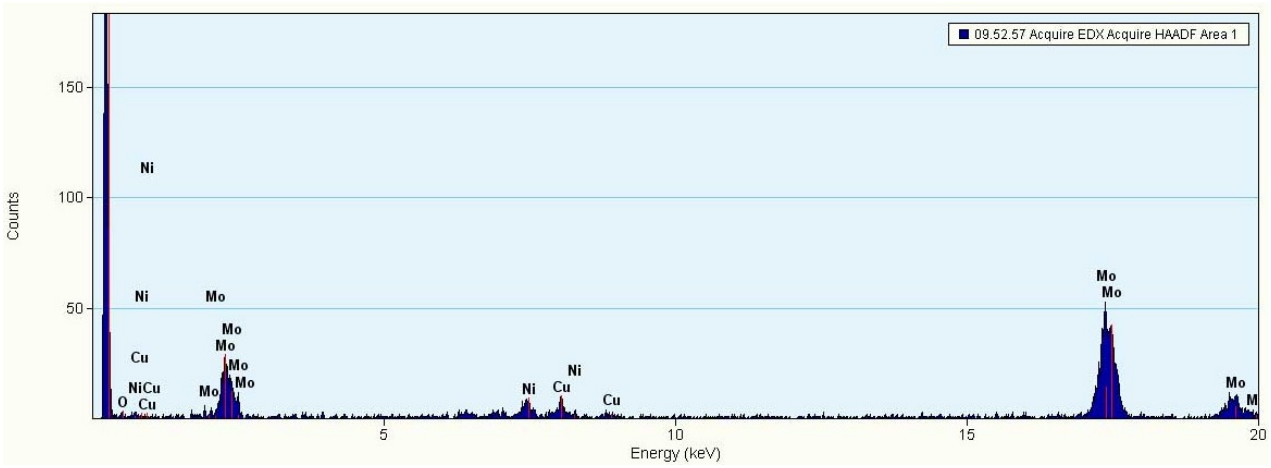

Figure S3. STEM-EDX spectrum of the as-prepared p-$Ni_{1-x}Cu_xO$ NWs. The Mo signals stem from the molybdenum grid used for TEM imaging.

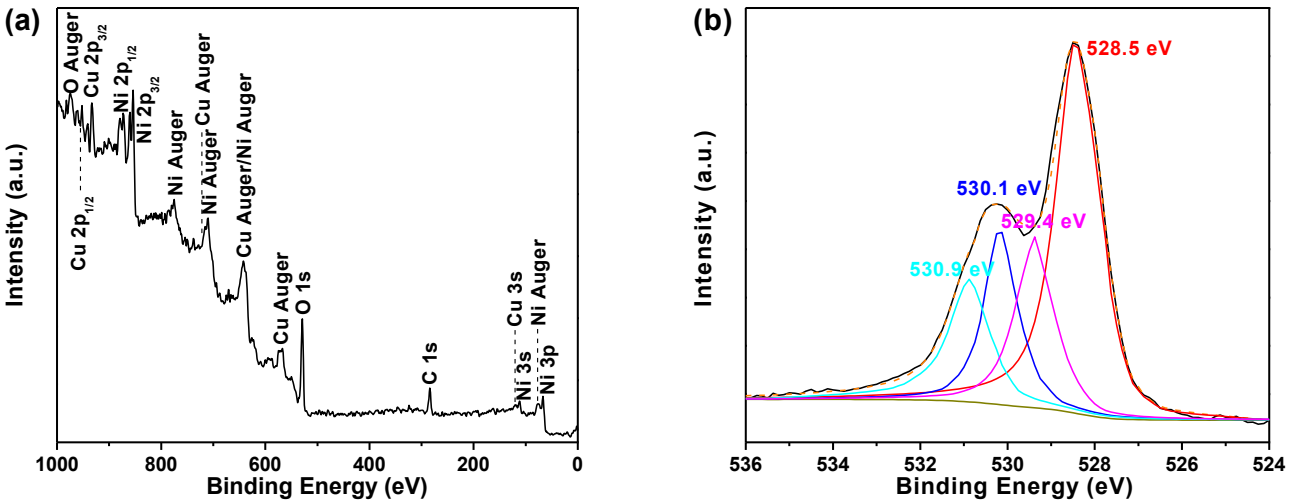

Figure S4. XPS spectra collected from the p-$Ni_{1-x}Cu_xO$ NWs. (a) XPS survey spectrum and (b) O 1s detail spectra.

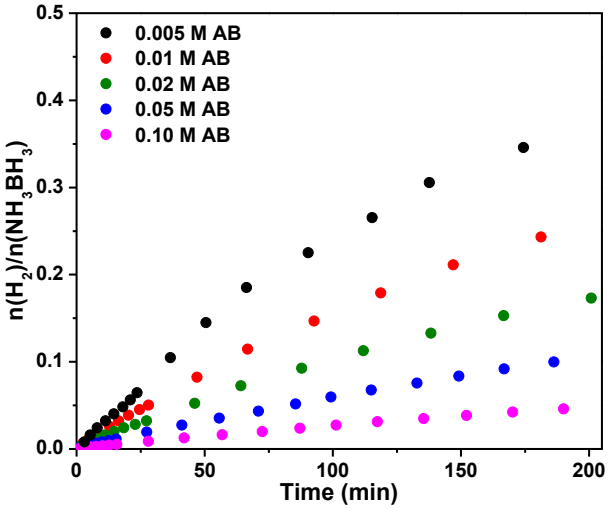

Figure S5. Stoichiometric hydrogen evolution versus time for the hydrolysis of AB ($NH_3BH_3(aq) + 2H_2O = NH_4BO_2(aq) + 3H_2(g)$) over p-$Ni_{1-x}Cu_xO$/CFP (1 × 2 cm^2, loading: 0.8 mg cm^{-2}) in 50 mL of 0.1 M KOH solution containing AB at a different concentration.

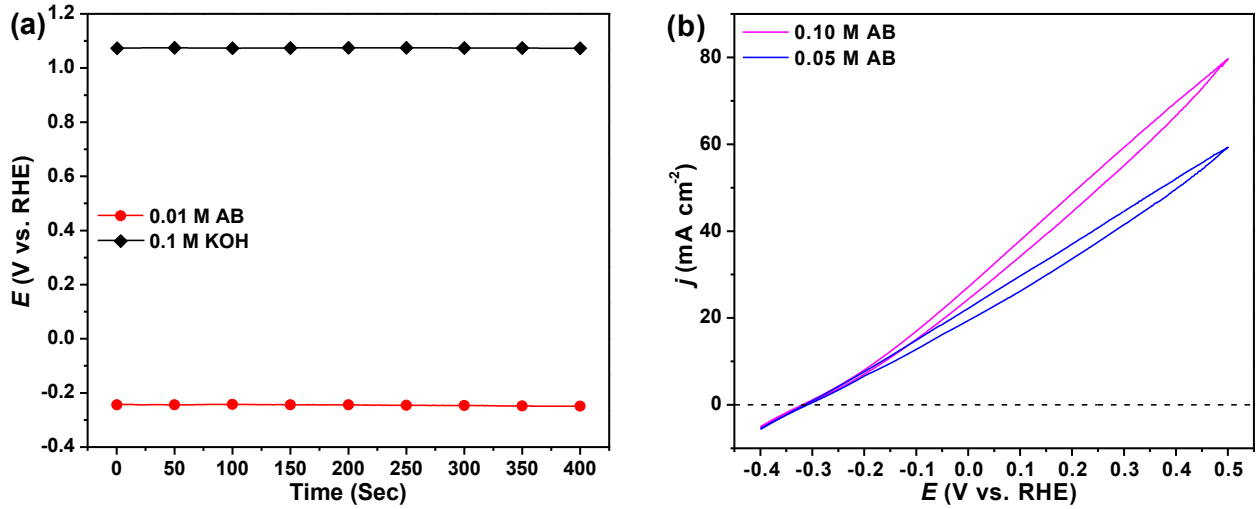

Figure S6. (a) The plots of open circuit potential (OCP) *versus* time recorded for the p-$Ni_{1-x}Cu_xO$/CFP electrode in 0.1 M KOH supporting electrolyte (OCP = 1.074 V_{RHE}) and in 0.1 M KOH electrolyte containing 0.01 M AB (OCP = −0.238 V_{RHE}). (b) CVs recorded in a wider potential range from −0.4 to 0.5 V_{RHE} in 0.1 M KOH electrolyte containing 0.05 and 0.1 M AB.

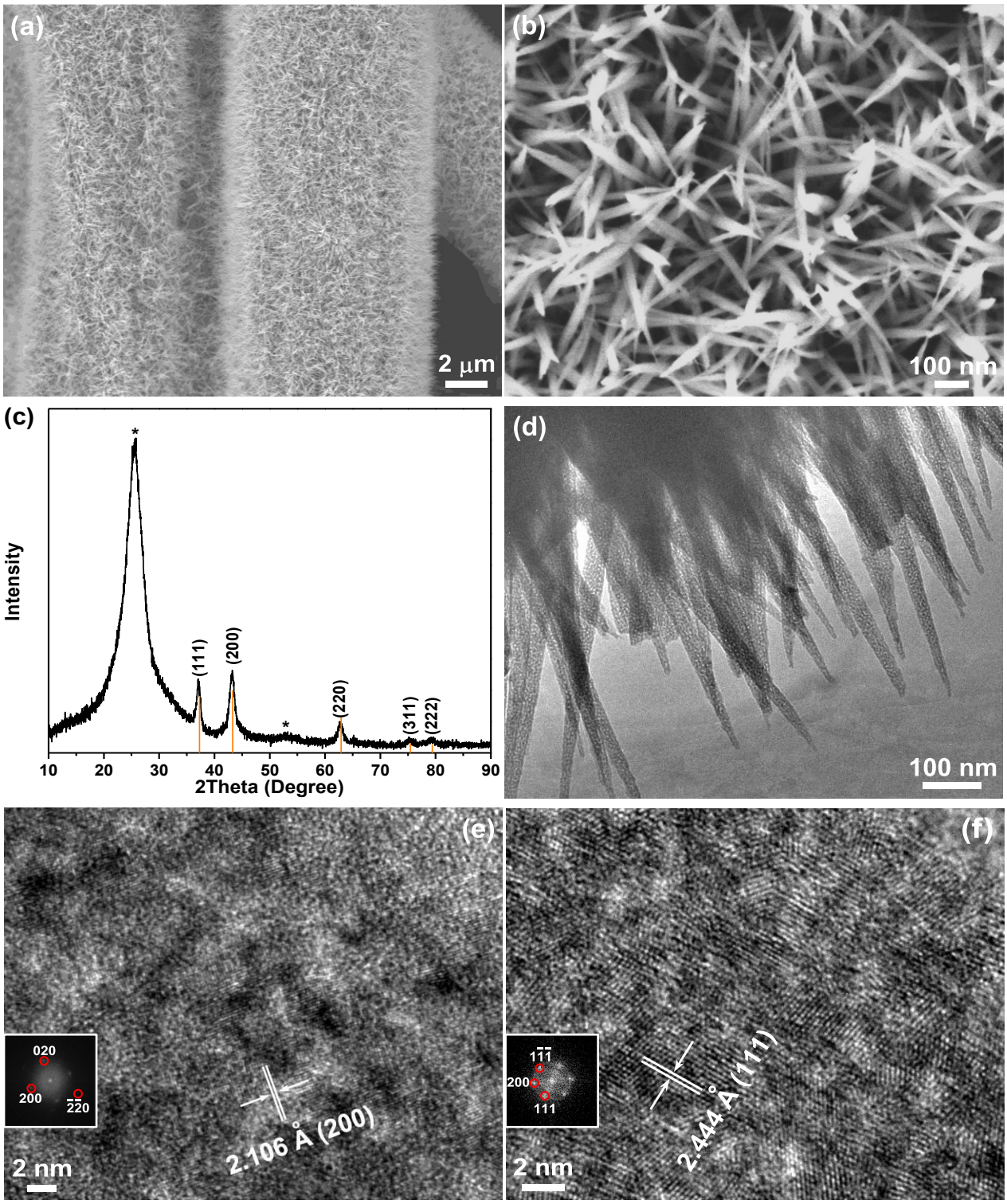

Figure S7. (a) Over-view and (b) zoom-in view SEM images, and (c) XRD pattern of the p-$Ni_{1-x}Cu_xO$/CFP electrode obtained after CP measurement at a j of 50 mA cm^{-2} for the ABOR over a period of 100 h. (d) TEM and (e and f) HRTEM images of the scratched p-$Ni_{1-x}Cu_xO$ NWs from the above tested p-$Ni_{1-x}Cu_xO$/CFP electrode. For comparison, the intensities and positions for the NiO reference are given in panel (c) according to the JCPDF database (JCPDF No. 04-0835, red lines at the bottom).

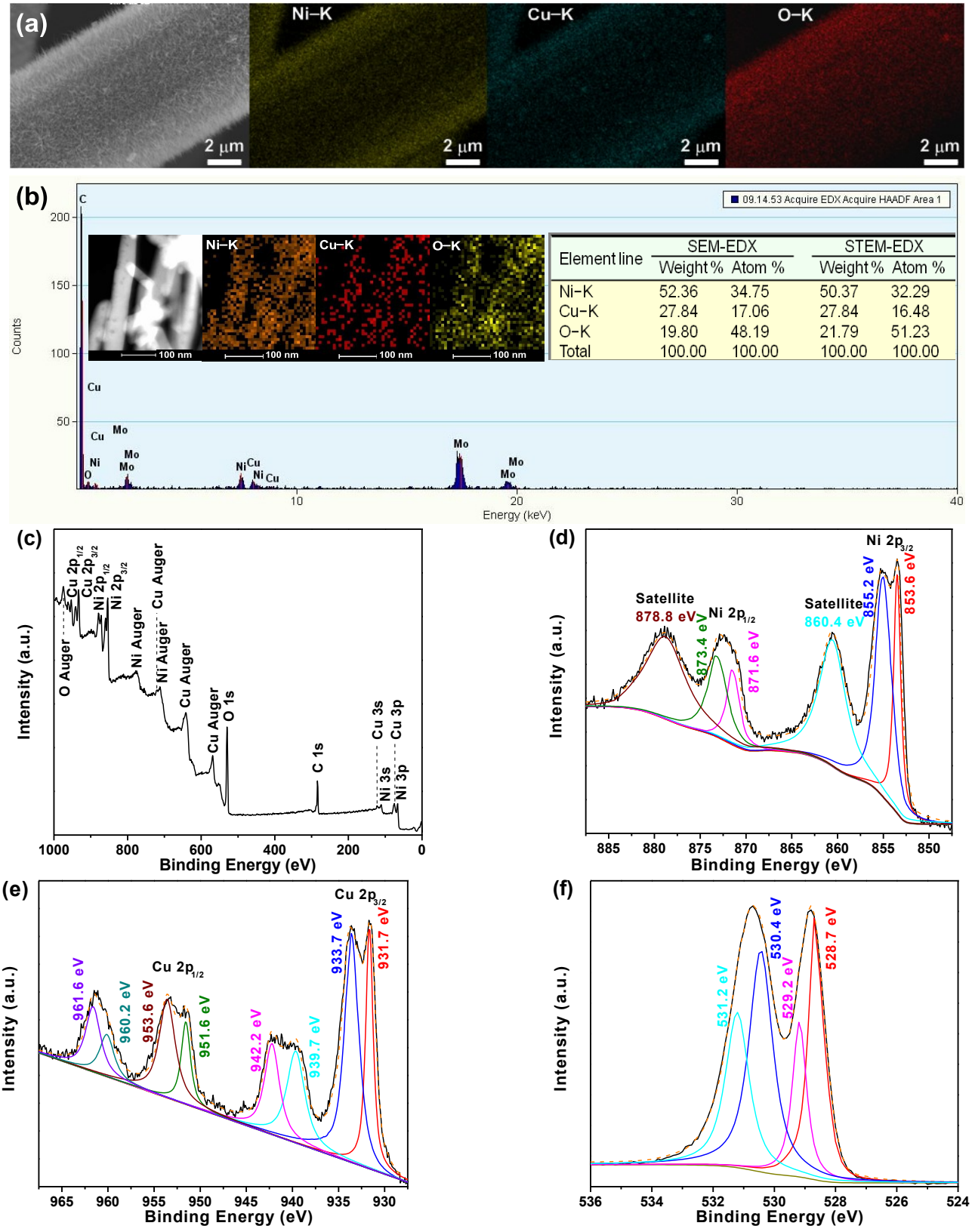

Figure S8. (a) A typical SEM and the corresponding SEM-EDX elemental mapping images of the p-$Ni_{1-x}Cu_xO$/CFP electrode obtained after the CP measurement at a *j* of 50 mA cm^{-2} for the ABOR over a period of 100 h. (b) STEM-EDX spectrum, (c) XPS survey spectrum, (d) Ni 2p, (e) Cu 2p, and (f) O 1s high-resolution spectra of the scratched p-$Ni_{1-x}Cu_xO$ NWs from the above tested p-$Ni_{1-x}Cu_xO$/CFP electrode. The Mo signals stem from the molybdenum grid used for TEM characterization. The insets in panel (b) show a HAADF-STEM image (the leftmost) and the corresponding HAADF-STEM-EDX elemental mapping images (the rest left three) and the chemical compositions (the right).

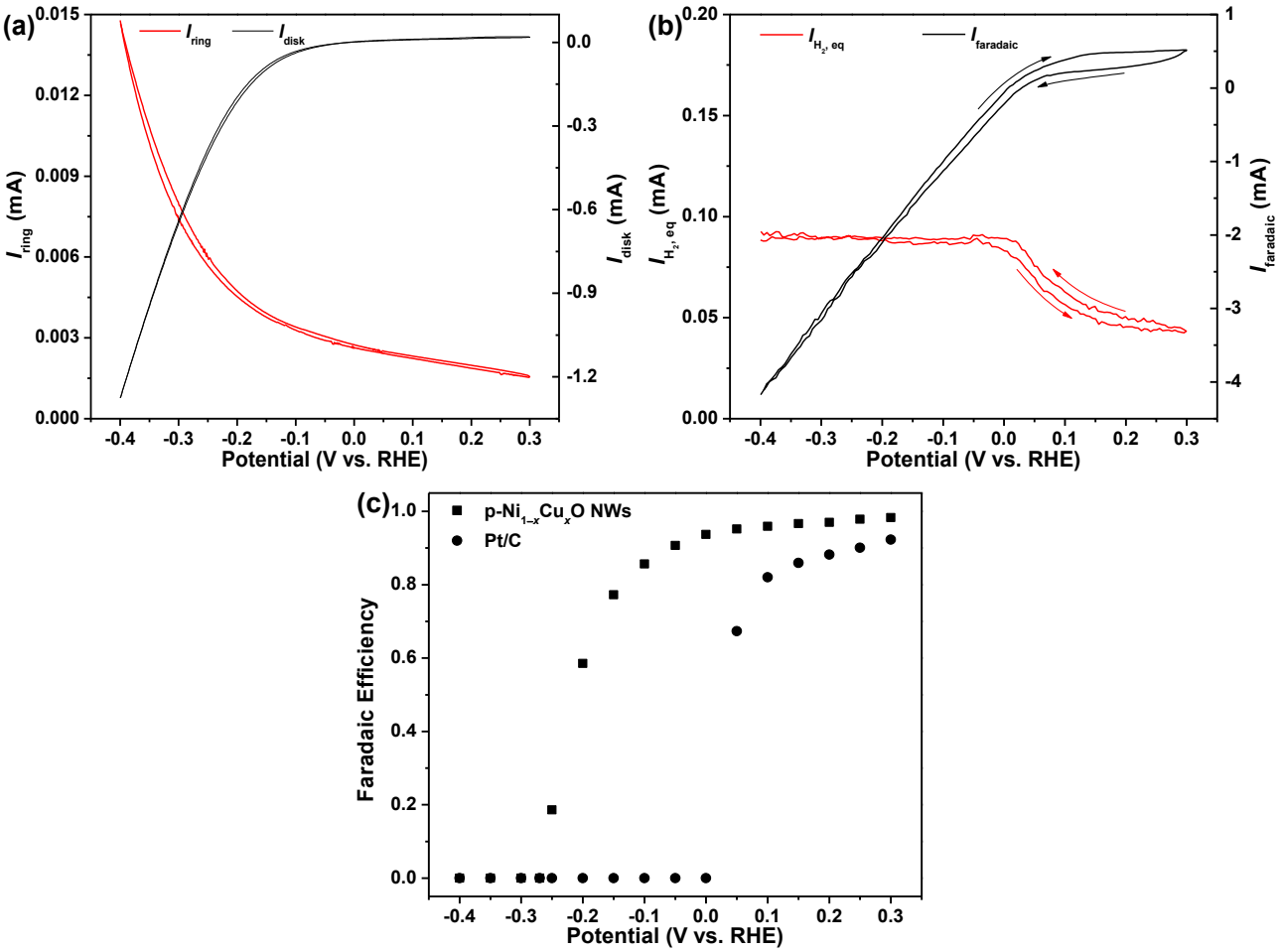

Figure S9. (a) RRDE measurements of the faradaic current for the HER (disk) and the faradaic current for the HOR (ring) of the evolved H_2 for the p-$Ni_{1-x}Cu_xO$ NWs electrocatalyst in 0.1 M KOH electrolyte. The potential applied on gold ring electrode was constant at 0.025 V_{RHE}. The CVs were recorded at a rotating rate of 1600 rpm. (b) The ABOR faradaic current and equivalent HER current ($I_{H2,eq}$) for H_2 (m/z = 2) detection obtained during DEMS measurements of CV for Pt/C in 0.1 M KOH electrolyte containing 0.01 M AB. (c) Plots of the faradaic efficiency versus potential for p-$Ni_{1-x}Cu_xO$ NWs and Pt/C.

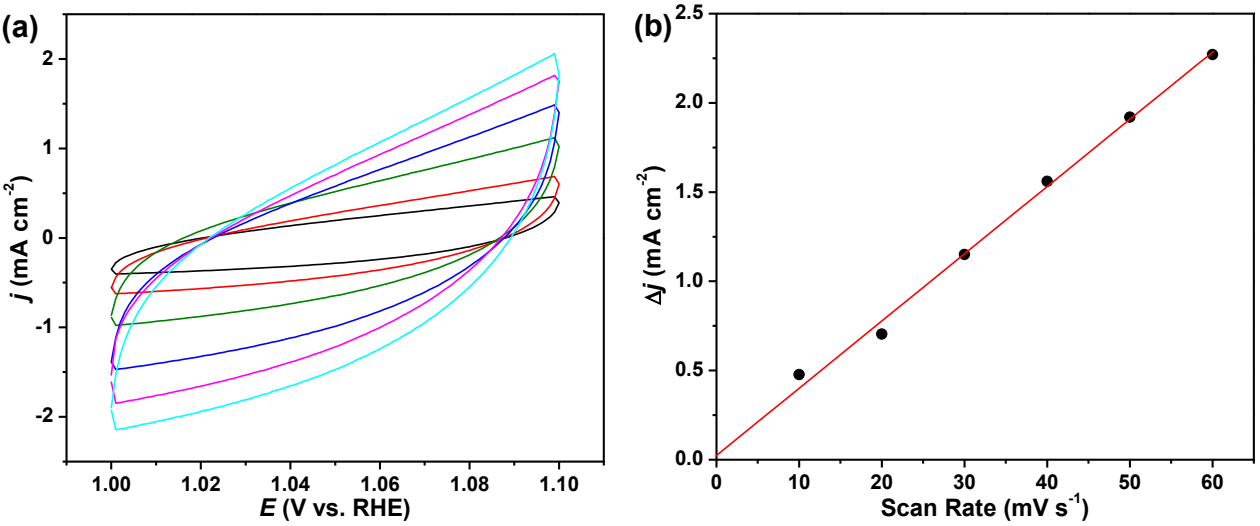

Figure S10. (a) CVs of the p-$Ni_{1-x}Cu_xO$/CFP electrode, which are used to estimate the double layer capacitances (C_{dl}). Scan rates from 10, 20, 30, 40, and 50 mV s^{-1} were chosen. (b) The capacitance currents vs. scan rate for the p-$Ni_{1-x}Cu_xO$/CFP electrode.

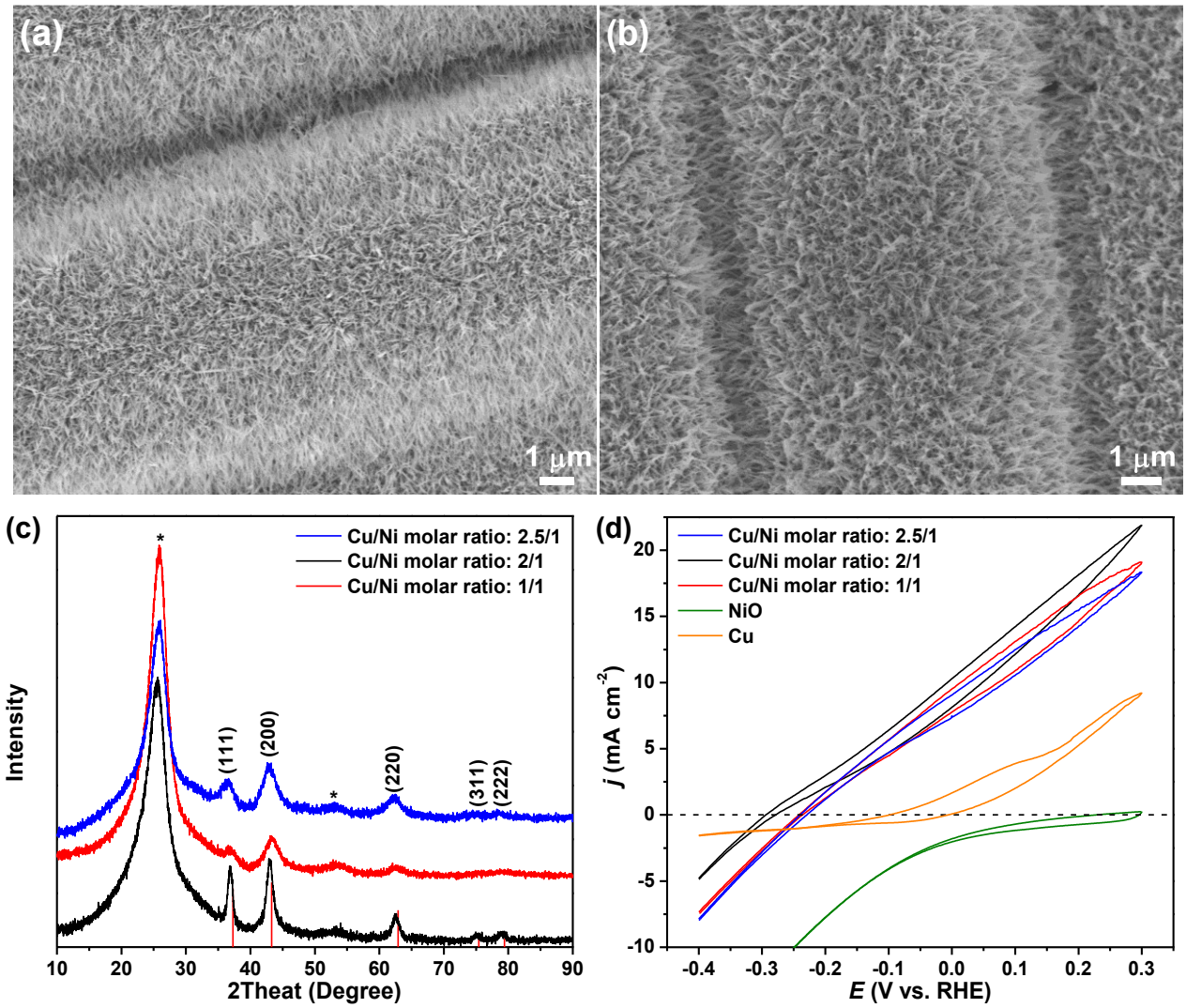

Figure S11. SEM images of the p-$Ni_{1-x}Cu_xO$/CFP electrodes prepared with a Cu/Ni precursor molar ratio of (a) 1 : 1 and (b) 2.5 : 1. (c) The corresponding XRD patterns of the $Ni_{1-x}Cu_xO$/CFP electrodes prepared at different Cu/Ni precursor molar ratios. For comparison, the intensities and positions for the NiO reference are presented based on the JCPDF database (JCPDF No. 04-0835, red lines at the bottom). The Ni : Cu : O atomic ratio is determined to be 2.1 : 0.9 : 3 or 1.9 : 1.1 : 3 both in the bulk and at the surface of the p-$Ni_{1-x}Cu_xO$ NWs sample obtained by the Cu/Ni precursor molar ratio of 1 : 1 or 2.5 : 1, respectively, by STEM-EDX and XPS quantitative analyses (the data are not shown for brevity). (d) The comparison of CVs obtained from the p-$Ni_{1-x}Cu_xO$/CFP electrodes prepared at different Cu/Ni precursor molar ratios, NiO NWs/CFP, and Cu electrodes (a clean static Cu plate, 0.5 × 1 cm^2, polished with 0.3 and 0.05 μm alumina slurries) recorded in 0.1 M KOH electrolyte containing 0.02 M AB.

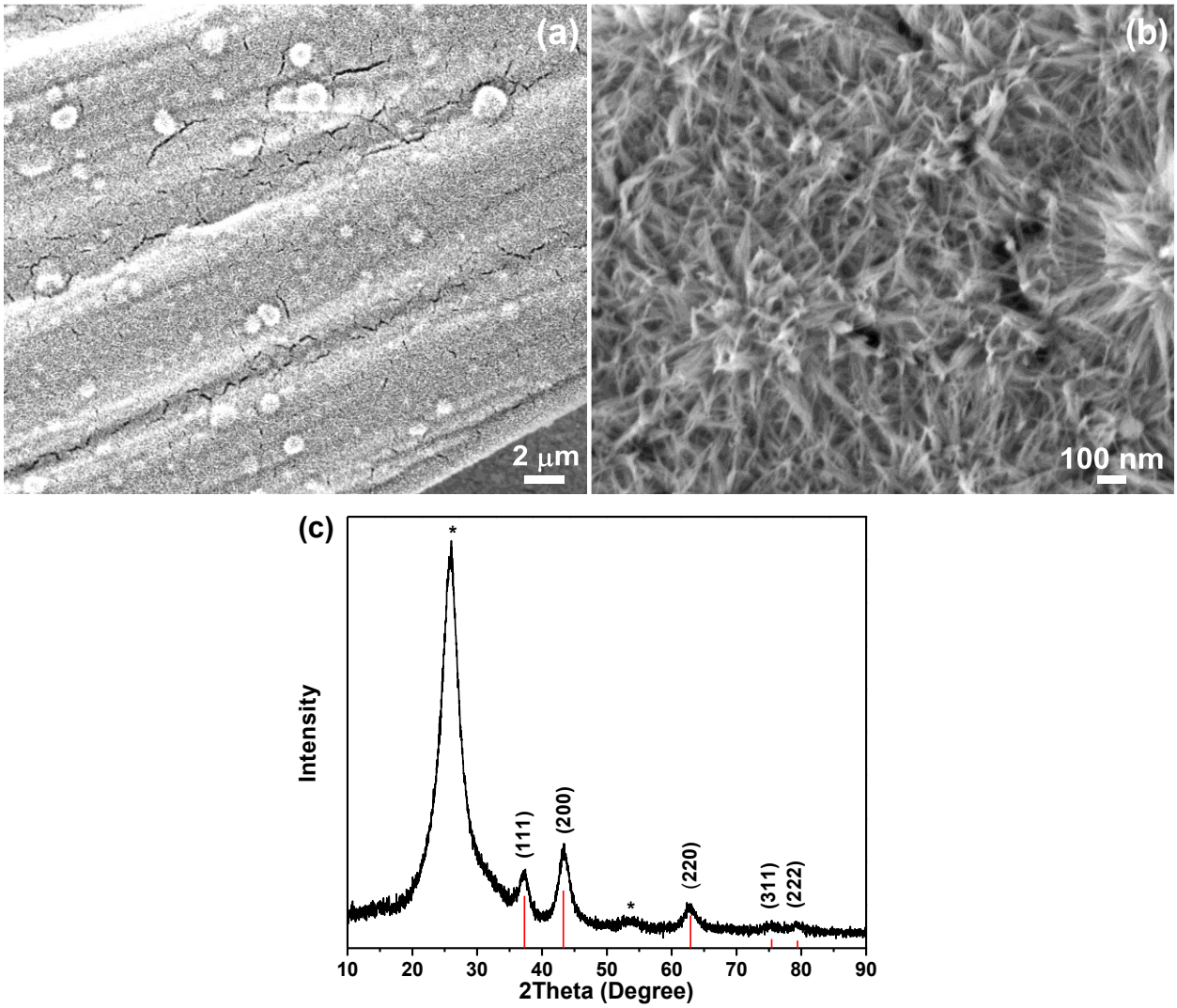

Figure S12. (a) Low- and (b) high-magnification SEM images and (c) XRD pattern of the NiO NWs grown on CFP. For comparison, the intensities and positions for the NiO reference are presented based on the JCPDF database (JCPDF No. 04-0835, red lines at the bottom).

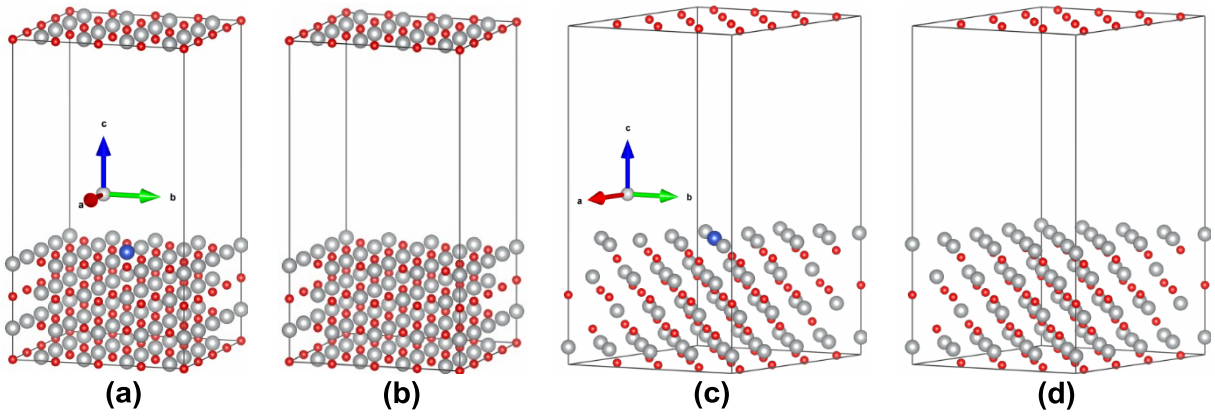

Figure S13. Relaxed GGA geometry of (a) the Cu-doped NiO(100), (b) NiO(100), (c) Cu-doped NiO(111), and (d) NiO(111) systems.

Table S1. Comparison of electrocatalytic parameters of the p-$Ni_{1-x}Cu_xO$/CFP anode and other electrodes reported in the literature for ABOR.

Samples	Onset potential (V vs. RHE)	Oxidation current [a] ($mA\ cm^{-2}$)	Catalyst loading ($mg\ cm^{-2}$)	Electrolyte solution	scan rate ($mV\ s^{-1}$)	Ref
Ag(30 wt%)/C	−0.104	~20 (0.446 V)	not mentioned	0.1 M AB + 2 M KOH	5	3
Au disk	*ca*. −0.03	~407 (0.873 V)	not mentioned	0.04 M AB + 1 M NaOH	100	10
NPG wire array	−0.230	13.1 (0.570 V)	not mentioned	0.02 M AB + 1 M NaOH	10	13
Fe@Pt NPs/C	*ca*. −0.090[b]	6.0 (0.370 V)[b] 7.5 (0.870 V)[b]	0.0246 for Pt	0.01 M AB + 1 M NaOH	10	15
Pt/C	*ca*. −0.060[c]	30 (0.669 V)[c]	0.5 for Pt	0.01 M AB + 1 M NaOH	25	16
Pd/C	*ca*. −0.275[c]	30 (0.641 V)[c]	0.5 for Pd	0.01 M AB + 1 M NaOH	25	16
Ni_3Co/C	−0.090[b]	5 (0.3 V)[b]	0.255 for Ni_3Co	5 mM AB + 0.1 M NaOH	10	17
Ni_3Pd/C	−0.030[b]	10 (0.5 V)[b]	0.255 for Ni_3Pd	5 mM AB + 0.1 M NaOH	10	17
Ni_3Ag/C	−0.050[b]	6.3 (0.5 V)[b]	0.255 for Ni_3Ag	5 mM AB + 0.1 M NaOH	10	17
$Ni_{1-x}Cu_xO$/CFP[d]	−0.267	4.65 (0.3 V)	0.86	0.01 M AB + 0.1 M KOH	10	This work

[a] The potential value corresponds to the oxidation current density and is expressed on the RHE scale. [b] The values are obtained on the electrode at a rotation rate of 1600 rpm. [c] The values are obtained on the electrode at a rotation rate of 1000 rpm. [d] Also see Table 1.

Table S2. Reaction energies ($\Delta E = \Sigma E_{products} - \Sigma E_{reactants}$), zero point energy corrections (ΔZPE), entropic contributions ($T\Delta S$) of closed shell molecules on the (100) and (111) surfaces of $Ni_{1-x}Cu_xO$ and NiO at $T = 298.15$ K.

Elementary reactions	Catalyst surfaces	ΔE (eV)	ΔZPE (eV)	TΔS (eV)
$NH_3BH_3(g) + * = NH_3BH_3*$	$Ni_{1-x}Cu_xO(100)$	−1.68	0.17	−0.61
	NiO(100)	−1.39	0.15	−0.61
	$Ni_{1-x}Cu_xO(111)$	−1.57	0.18	−0.61
	NiO(111)	−1.23	0.17	−0.61
$NH_3BH_3* + OH^- = NH_3BH_3OH^-*$	$Ni_{1-x}Cu_xO(100)$	0.16	0.08	−0.54
	NiO(100)	0.63	0.07	−0.54
	$Ni_{1-x}Cu_xO(111)$	0.18	0.10	−0.54
	NiO(111)	0.73	0.06	−0.54
$NH_3BH_3OH^-* = NH_3* + BH_3OH^-*$	$Ni_{1-x}Cu_xO(100)$	−0.53	−0.03	0
	NiO(100)	−0.19	−0.03	0
	$Ni_{1-x}Cu_xO(111)$	−0.42	−0.03	0
	NiO(111)	−0.07	−0.02	0
$BH_3OH^-* + OH^- = BH_3(OH)_2^{2-}*$	$Ni_{1-x}Cu_xO(100)$	0.30	0.05	−0.54
	NiO(100)	0.83	0.06	−0.54
	$Ni_{1-x}Cu_xO(111)$	0.42	0.07	−0.54
	NiO(111)	0.88	0.07	−0.54
$BH_3(OH)_2^{2-}* = BH_3(OH)_2^-* + e^-$	$Ni_{1-x}Cu_xO(100)$	−0.29	−0.03	0.04
	NiO(100)	0.92	−0.02	0.04
	$Ni_{1-x}Cu_xO(111)$	−0.22	−0.03	0.04
	NiO(111)	1.05	−0.01	0.04
$BH_3(OH)_2^-* = BH_2(OH)_2^-* + H*$	$Ni_{1-x}Cu_xO(100)$	−1.26	−0.01	0
	NiO(100)	−0.56	−0.01	0
	$Ni_{1-x}Cu_xO(111)$	−1.05	−0.01	0
	NiO(111)	−0.38	−0.01	0
$H* + OH^- = H_2O + e^-$	$Ni_{1-x}Cu_xO(100)$	−0.41	0.15	0.09
	NiO(100)	−0.28	0.15	0.09
	$Ni_{1-x}Cu_xO(111)$	−0.33	0.15	0.09
	NiO(111)	−0.14	0.15	0.09
$BH_2(OH)_2^-* + OH^- = BH_2(OH)_3^{2-}*$	$Ni_{1-x}Cu_xO(100)$	−0.06	0.06	−0.54
	NiO(100)	0.15	0.08	−0.54
	$Ni_{1-x}Cu_xO(111)$	0.05	0.08	−0.54
	NiO(111)	0.31	0.09	−0.54
$BH_2(OH)_3^{2-}* = BH_2(OH)_3^-* + e^-$	$Ni_{1-x}Cu_xO(100)$	−0.62	−0.02	0.04
	NiO(100)	0.57	−0.02	0.04
	$Ni_{1-x}Cu_xO(111)$	−0.55	−0.01	0.04
	NiO(111)	0.78	−0.02	0.04
$BH_2(OH)_3^-* = BH(OH)_3^-* + H*$	$Ni_{1-x}Cu_xO(100)$	−1.56	−0.02	0
	NiO(100)	−0.77	−0.01	0
	$Ni_{1-x}Cu_xO(111)$	−1.39	−0.02	0
	NiO(111)	−0.62	−0.01	0
$H* + OH^- = H_2O + e^-$	$Ni_{1-x}Cu_xO(100)$	−0.41	0.15	0.09
	NiO(100)	−0.28	0.15	0.09
	$Ni_{1-x}Cu_xO(111)$	−0.33	0.15	0.09
	NiO(111)	−0.14	0.15	0.09
$BH(OH)_3^-* + OH^- = BH(OH)_4^{2-}*$	$Ni_{1-x}Cu_xO(100)$	−0.25	0.05	−0.54
	NiO(100)	0.09	0.06	−0.54
	$Ni_{1-x}Cu_xO(111)$	−0.15	0.04	−0.54
	NiO(111)	0.23	0.04	−0.54
$BH(OH)_4^{2-}* = BH(OH)_4^-* + e^-$	$Ni_{1-x}Cu_xO(100)$	−0.79	−0.02	0.04
	NiO(100)	0.35	−0.01	0.04
	$Ni_{1-x}Cu_xO(111)$	−0.73	−0.02	0.04
	NiO(111)	0.43	−0.01	0.04
$BH(OH)_4^-* = B(OH)_4^-* + H*$	$Ni_{1-x}Cu_xO(100)$	−1.14	−0.02	0
	NiO(100)	−0.82	−0.02	0
	$Ni_{1-x}Cu_xO(111)$	−1.03	−0.02	0
	NiO(111)	−0.71	−0.01	0
$H* + OH^- = H_2O + e^-$	$Ni_{1-x}Cu_xO(100)$	−0.41	0.15	0.09
	NiO(100)	−0.28	0.15	0.09
	$Ni_{1-x}Cu_xO(111)$	−0.33	0.15	0.09
	NiO(111)	−0.14	0.15	0.09

Table S3. DFT computed free energies (ΔG) for the elementary reaction steps in the ABOR on the (100) and (111) surfaces of $Ni_{1-x}Cu_xO$ and NiO at $T = 298.15$ K and a different external bias U.[a]

Elementary reaction steps (formula of ΔG)	bias U (V_{NHE})	ΔG (eV)			
		$Ni_{1-x}Cu_xO(100)$	NiO(100)	$Ni_{1-x}Cu_xO(111)$	NiO(111)
$NH_3BH_3(g) + * = NH_3BH_3*$	−0.40	−0.90	−0.63	−0.78	−0.45
($\Delta G_1 = E_{NH_3BH_3*} - E_* - E_{NH_3BH_3(g)} +$	−0.25	−0.90	−0.63	−0.78	−0.45
$\Delta ZPE_1 - T\Delta S_1$)[b]	0.050	−0.90	−0.63	−0.78	−0.45
$NH_3BH_3* + OH^- = NH_3BH_3OH^-*$	−0.40	0.84	1.30	0.88	1.39
($\Delta G_2 = E_{NH_3BH_3OH^-*} - E_{BH_3OH^-*} - E_{OH^-} +$	−0.25	0.84	1.30	0.88	1.39
$\Delta ZPE_2 - T\Delta S_2 - k_BT\ln[OH^-]$)	0.050	0.84	1.30	0.88	1.39
$NH_3BH_3OH^-* = NH_3* + BH_3OH^-*$	−0.40	−0.56	−0.22	−0.45	−0.09
($\Delta G_3 = E_{NH_3*} + E_{BH_3OH^-*} - E_{NH_3BH_3OH^-*}$	−0.25	−0.56	−0.22	−0.45	−0.09
$+ \Delta ZPE_3 - T\Delta S_3$)	0.050	−0.56	−0.22	−0.45	−0.09
$BH_3OH^-* + OH^- = BH_3(OH)_2{}^{2-}*$	−0.40	0.95	1.49	1.09	1.55
($\Delta G_4 = E_{BH_3(OH)_2{}^{2-}*} - E_{BH_3OH^-*} - E_{OH^-} +$	−0.25	0.95	1.49	1.09	1.55
$\Delta ZPE_4 - T\Delta S_4 - k_BT\ln[OH^-]$)	0.050	0.95	1.49	1.09	1.55
$BH_3(OH)_2{}^{2-}* = BH_3(OH)_2{}^-* + e^-$	−0.40	0.040	1.26	0.11	1.40
($\Delta G_5 = E_{BH_3(OH)_2{}^-*} - E_{BH_3(OH)_2{}^{2-}*} - eU +$	−0.25	−0.11	1.11	−0.04	1.25
$\Delta ZPE_5 - T\Delta S_5$)	0.050	−0.41	0.81	−0.34	0.95
$BH_3(OH)_2{}^-* = BH_2(OH)_2{}^-* + H*$	−0.40	−1.27	−0.57	−1.06	−0.39
($\Delta G_{6a} = E_{BH_2(OH)_2{}^-*} + E_{H*} - E_{BH_3(OH)_2{}^-*}$	−0.25	−1.27	−0.57	−1.06	−0.39
$+ \Delta ZPE_{6a} - T\Delta S_{6a}$)	0.050	−1.27	−0.57	−1.06	−0.39
$H* + OH^- = H_2O + e^-$	−0.40	0.11	0.24	0.19	0.38
($\Delta G_{6b} = E_{H_2O} - E_{H*} - E_{OH^-} - eU +$	−0.25	−0.041	0.089	0.039	0.23
$\Delta ZPE_{6b} - T\Delta S_{6b} - k_BT\ln[OH^-]$)	0.050	−0.34	−0.21	−0.26	−0.071
$BH_2(OH)_2{}^-* + OH^- = BH_2(OH)_3{}^{2-}*$	−0.40	0.60	0.83	0.73	1.00
($\Delta G_7 = E_{BH_2(OH)_3{}^{2-}*} - E_{BH_2(OH)_2{}^-*} - E_{OH^-}$	−0.25	0.60	0.83	0.73	1.00
$+ \Delta ZPE_7 - T\Delta S_7 - k_BT\ln[OH^-]$)	0.050	0.60	0.83	0.73	1.00
$BH_2(OH)_3{}^{2-}* = BH_2(OH)_3{}^-* + e^-$	−0.40	−0.28	1.01	−0.20	1.22
($\Delta G_8 = E_{BH_2(OH)_3{}^-*} - E_{BH_2(OH)_3{}^{2-}*} - eU$	−0.25	−0.43	0.86	−0.35	1.07
$+ \Delta ZPE_8 - T\Delta S_8$)	0.050	−0.73	0.56	−0.65	0.77
$BH_2(OH)_3{}^-* = BH(OH)_3{}^-* + H*$	−0.40	−1.58	−0.78	−1.41	−0.63
($\Delta G_{9a} = E_{BH(OH)_3{}^-*} + E_{H*} - E_{BH_2(OH)_3{}^-*}$	−0.25	−1.58	−0.78	−1.41	−0.63
$+ \Delta ZPE_{9a} - T\Delta S_{9a}$)	0.050	−1.58	−0.78	−1.41	−0.63
$H* + OH^- = H_2O + e^-$	−0.40	0.11	0.24	0.19	0.38
($\Delta G_{9b} = E_{H_2O} - E_{H*} - E_{OH^-} - eU +$	−0.25	−0.041	0.089	0.039	0.23
$\Delta ZPE_{9b} - T\Delta S_{9b} - k_BT\ln[OH^-]$)	0.050	−0.34	−0.21	−0.26	−0.071
$BH(OH)_3{}^-* + OH^- = BH(OH)_4{}^{2-}*$	−0.40	0.41	0.75	0.49	0.87
($\Delta G_{10} = E_{BH(OH)_4{}^{2-}*} - E_{BH(OH)_3{}^-*} - E_{OH^-}$	−0.25	0.41	0.75	0.49	0.87
$+ \Delta ZPE_{10} - T\Delta S_{10} - k_BT\ln[OH^-]$)	0.050	0.41	0.75	0.49	0.87
$BH(OH)_4{}^{2-}* = BH(OH)_4{}^-* + e^-$	−0.40	−0.45	0.80	−0.39	0.88
($\Delta G_{11} = E_{BH(OH)_4{}^-*} - E_{BH(OH)_4{}^{2-}*} - eU$	−0.25	−0.60	0.65	−0.54	0.73
$+ \Delta ZPE_{11} - T\Delta S_{11}$)	0.050	−0.90	0.35	−0.84	0.43
$BH(OH)_4{}^-* = B(OH)_4{}^-* + H*$	−0.40	−1.16	−0.84	−1.05	−0.72
($\Delta G_{12a} = E_{B(OH)_4{}^-*} + E_{H*} - E_{BH(OH)_4{}^-*}$	−0.25	−1.16	−0.84	−1.05	−0.72
$+ \Delta ZPE_{12a} - T\Delta S_{12a}$)	0.050	−1.16	−0.84	−1.05	−0.72
$H* + OH^- = H_2O + e^-$	−0.40	0.11	0.24	0.19	0.38
($\Delta G_{12b} = E_{H_2O} - E_{H*} - E_{OH^-} - eU +$	−0.25	−0.041	0.089	0.039	0.23
$\Delta ZPE_{12b} - T\Delta S_{12b} - k_BT\ln[OH^-]$)	0.05	−0.34	−0.21	−0.26	−0.071

[a] For the involved Faradaic steps, the reaction energies are reported at −0.40, −0.25, and 0.050 V_{NEH} and at pH 13. The applied voltage is accounted for by adding a constant energy term $-eU$ to the reaction energies of reactions 5, 6b, 8, 9b, 11, and 12b with respect to the normal hydrogen electrode (NHE). [b] $E_{NH_3BH_3*}$ and E_* are the computed DFT energies of the surface with adsorbed AB* and pure surface, respectively. Likewise, the terms in other formula have the similar meanings. $E_{NH_3BH_3(g)}$ is the computed DFT energy of AB molecule in the gas phase.

References

1. Birry, L.; Lasia, A. Studies of the Hydrogen Evolution Reaction on Raney Nickel—Molybdenum Electrodes. *J. Appl. Electrochem*. **2004**, *34*, 735−749.
2. Herraiz-Cardona, I.; Ortega, E.; Pérez-Herranz, V. Impedance Study of Hydrogen Evolution on Ni/Zn and Ni–Co/Zn Stainless Steel Based Electrodeposits. *Electrochim. Acta* **2011**, *56*, 1308−1315.
3. Lačnjevac, U.; Vasilić, R.; Tokarski, T.; Cios, G.; Żabiński, P.; Elezović, N.; Krstajić, N. Deposition of Pd Nanoparticles on the Walls of Cathodically Hydrogenated TiO_2 Nanotube Arrays via Galvanic Displacement: A Novel Route to Produce Exceptionally Active and Durable Composite Electrocatalysts for Cost-Effective Hydrogen Evolution. *Nano Energy* **2018**, *47*, 527−538.
4. Yu, Z.-Y.; Duan, Y.; Gao, M.-R.; Lang, C.-C.; Zheng, Y.-R.; Yu, S.-H. A One-Dimensional Porous Carbon-Supported Ni/Mo_2C Dual Catalyst for Efficient Water Splitting. *Chem. Sci*. **2017**, *8*, 968−973.
5. Xu, X.; Liang, H.; Ming, F.; Qi, Z.; Xie, Y.; Wang, Z. Prussian Blue Analogues Derived Penroseite (Ni,Co)Se_2 Nanocages Anchored on 3D Graphene Aerogel for Efficient Water Splitting. *ACS Catal*. **2017**, *7*, 6394−6399.
6. McCrory, C. C. L.; Jung, S.; Peters, J. C.; Jaramillo, T. F. Benchmarking Heterogeneous Electrocatalysts for the Oxygen Evolution Reaction. *J. Am. Chem. Soc*. **2013**, *135*, 16977−16987.